Journal Name

ARTICLE TYPE

Cite this: DOI: 00.0000/xxxxxxxxxx

Direct observation of long chain enrichment in flow-induced nuclei from molecular dynamics simulations of bimodal blends

Muhammad Anwar,[a,‡] and Richard S. Graham *[a,¶]

Received Date
Accepted Date

DOI: 00.0000/xxxxxxxxxx

Modelling of flow-induced nucleation in polymers suggest that long chains are enriched in nuclei, relative to their melt concentration. This enrichment has important consequences for the nucleation rate and mechanism, but cannot be directly observed with current experimental techniques. Instead, we ran united atom molecular dynamics simulations of bimodal polyethylene blends, comprising linear chains at a 50:50 mix of long (1000 carbon) and short (500-125 carbon) chains, under shear flow. We developed a method to extract the nucleus composition during a transient start-up flow. Our simulations show significant and systematic enrichment of long-chains for all nucleus sizes up to and beyond the critical nucleus. This enrichment is quantitatively predicted by the recent polySTRAND model [Read *et al.* Phys. Rev. Lett. 2020, 124,147802]. The same model parameters also correctly capture the nucleus induction time in our simulations. All parameters of the model were fitted to a small subset of our data in which long chain enhancement was absent. We conclude that long-chain enrichment is central to the mechanism of flow-induced nucleation and that this enrichment must be captured to correctly predict the nucleation rate.

1 Introduction

Flow-induced crystallisation (FIC) in polymers[1–3] is a central problem in polymer science. Flow dramatically enhances the nucleation rate, leading to much faster crystallisation kinetics and, ultimately, controls the crystal morphology[4–13]. A predictive molecular understanding of polymer FIC would be enormously useful to the worldwide polymer processing industry, as it would enable control of crystalline properties through processing conditions. Despite extensive experimental progress a critical difficulty remains[14]: nucleation is extremely rapid and highly localised, meaning nucleation events cannot be observed directly in experiments. In such situations there is an important role for Molecular Dynamics (MD) simulations to complement experiments. The extremely high spatio-temporal resolution of MD simulations can inform models and distinguish between competing theoretical ideas. This emergent approach is particularly important in soft matter where wide spatiotemporal separations are common. Recent pioneering work on direct MD simulations of polymer nucleation during flow[15–17] has overcome the numerous technical barriers, allowing detailed observation of the key nucleation physics for monodisperse chains. Although recent work[18] has presented a method to estimate the critical nucleus volume from experiments, via the Hoffman and Lauritzen model[19], MD data provide significantly more detail, particularly under flow, and require essentially no model interpretation.

Unfortunately, the molecular weight and temperature ranges achievable in simulations are significantly below those of experiments and industrial processing[14,20]. Thus, recent work has focused on using MD to inform more coarse-grained approaches to polymer FIC[14], in order to reach the temperatures and molecular weights relevant to experiments and processing. There has been intense recent activity in this area[14–17,21–24]. The newly published polySTRAND[24] model integrates MD[15,22], kinetic Monte Carlo simulations[25,26] and thermodynamic modelling[27–29] to produce an analytic continuum model for flow induced nucleation in polymers. It accounts, in detail, for the effect of polydispersity on both flow and nucleation dynamics. In particular, long chains deform strongly and so attach more readily than shorter, less deformed chains. Consequently, the model predicts that, relative to their melt concentration, long chains are enriched in nuclei. Thus, multiple chain lengths cooperate in nontrivial ways to determine the nucleation barrier. This barrier height sets the nucleation rate via an exponential dependence and so correctly pre-

[a] *School of Mathematical Sciences, University of Nottingham, Nottingham, NG9 4DP, UK.*

‡ Present address: Department of Mechanical Engineering, Institute of Space Technology, Islamabad, Pakistan.

§ manwar18@gmail.com

¶Richard.Graham@nottingham.ac.uk

dicting the long chain enrichment is essential to quantitative FIC modelling. Hence, polydispersity plays a dominant role in FIC in both experiments and industrial polymer processing, where polydisperse melts are ubiquitous.

Long chain enrichment explains the experimentally observed super-exponential growth in the nucleation rate with shear rate[10]. However, scattering data by Kimata *et al.*[7] apparently contradict this. Their experiments demonstrated no over-representation of long chains in shish structures. However these experiments and the model pertain to different stages of the crystallisation process. The polySTRAND model predicts enrichment in nuclei around the critical size[24]. In contrast, post-nucleation growth is thermodynamically favourable so recruits all chains equally, giving the melt distribution in well-developed crystals. Consequently, there is a clear need for direct observation of the composition of flow-induced nuclei around the critical size. Unfortunately, this is beyond the spatio-temporal resolution of existing experimental techniques. Instead, we employ MD and exploit its extremely high spatio-temporal resolution to complement experiments. Prior flow-induced nucleation simulations in MD[15–17,22,23] have considered only monodisperse chains, which precludes long chain enrichment. In this work we present MD results from entangled bidisperse chains, of widely separated lengths. We choose this blend composition to provide the strongest possible long chain enrichment from a blend that is computationally tractable and for which both species are entangled. In our flow-induced nucleation simulations we observe significant and systematic enrichment of long-chains for all nucleus sizes up to and beyond the critical nucleus. We are able to quantitatively capture this enrichment with the polySTRAND model[24]. Our work provides a direct quantitative validation of this key model prediction[24], which is impossible with current experimental techniques.The same model parameters also correctly captures the nucleus induction time seen in our simulations. This shows that long-chain enrichment is central to the mechanism of flow-induced nucleation in polydisperse systems and that long-chain enrichment must be captured to correctly predict the nucleation rate.

2 Simulations

2.1 Force-field

We run simulations using a united atom model, which was proposed by Paul *et al.*[30] and then modified by Waheed *et al.*[31,32]. It has been used extensively by Rutledge and co-workers[15,33–35], Schilling and co-workers[17,36,37] and Graham and co-workers[22] to study crystallisation under quiescent and under flow conditions. In this model, CH_2 and CH_3 groups are represented by beads or "united atoms". These beads interact with each other via bonded and non-bonded potentials. The non-bonded interaction consists of Lennard Jones interactions and can be expressed by the following relation for a distance r_{ij} between monomers i and j:

$$\begin{aligned} U(r_{ij}) &= 4\varepsilon_{ij}[(\frac{\sigma_{ij}}{r_{ij}})^{12}-(\frac{\sigma_{ij}}{r_{ij}})^{6}], r_{ij} \leq 2.5\sigma_{ij} \\ U(r_{ij}) &= 0, r_{ij} > 2.5\sigma_{ij}. \end{aligned} \quad (1)$$

The bonded potential, which acts between monomers along the chain, consists of a harmonic bond potential

$$U(r_{ij}) = \frac{1}{2}K(r_{ij}-R)^2, \quad (2)$$

a harmonic bond angle potential

$$U(\theta) = \frac{1}{2}K_\theta(\theta-\theta_0)^2, \quad (3)$$

where θ is the angle between two consecutive bonds, and a dihedral potential

$$U(\phi,) = \frac{1}{2}[K_{1\phi}(1-\cos\phi)+K_{2\phi}(1-\cos 2\phi)+K_{3\phi}(1-\cos 3\phi)] \quad (4)$$

where ϕ is the dihedral angle defined by three consecutive bonds.

We provide parameters for all potentials in table 1. The model has been optimised using experimental data to reproduce the dynamical and structural properties of the melt, thermophysical properties such as the melting point, and the rotator phase crystal structure.

Table 1 Force-field parameters for our M simulations: all parameters are from[38], except for the Lennard Jones cutoff radius which is from[33].

Potential	Parameters
Harmonic bond	bond length = 1.53 Å K = 700 kcal/mol Å^2
Bond Angle	K_θ = 120 kcal/mol θ_0 = 109.5°
Dihedral	$K_{1\phi}$ = 1.6 kcal/mol $K_{2\phi}$ = -0.867 kcal/mol $K_{3\phi}$ = 3.24 kcal/mol
Lennard Jones	σ = 4.01 A° ε (CH_2-CH_2) = 0.112 kcal/mol ε (CH_3-CH_3) = 0.112 kcal/mol ε (CH_2-CH_3)= 0.112 kcal/mol Cut off = 2.5 σ

2.2 Order parameters

2.2.1 Crystallinity order parameter

We differentiate the crystalline regions from a melt using a crystallinity order parameter, which has been used recently by Schilling and co-workers[17,36,37] and in our previous work[22]. This order parameter is based on the local alignment of segments of chains.

- First of all, we create a neighbour list of every bead i, which contain neighbouring beads j within a cut-off radius of $r_c = 1.5\sigma$ of bead i. It is ensured that bead i and j do not belong to the same chain.

- We associate a unit vector $\hat{e}$ to every bead i pointing from the centre of the bead $i-1$ to the centre of the bead $i+1$. Then, we determine the angle between particle i and each of its neighbours j.

$$\theta_{ij} = \arccos(\hat{e}_i \cdot \hat{e}_j) \begin{cases} \leq 10^\circ \text{ “aligned”} \\ > 10^\circ \text{ “non-aligned”} \end{cases} . \quad (5)$$

Now, the beads having more “aligned” neighbours than the threshold value (8 monomers in our study) are defined as crystalline beads. This threshold value is determined from the analysis of the probability distribution of aligned neighbours in the bulk melt. We draw a probability distribution of aligned neighbours for an equilibrated melt and select the threshold number of aligned neighbours to be the value where the probability reaches zero on the right-hand side of the bell shape curve of the probability distribution. This shows that no melt particles in the system have more aligned neighbours than this threshold value. Hence, if any particle has more aligned neighbours than this threshold value, it is a crystalline particle.

- Finally, the clusters of crystalline particles are identified using a standard clustering algorithm. The crystalline clusters in the system are identified by picking a random bead in the system and checking if it is crystalline or not. If it is crystalline, we count it as the first bead of this cluster and examine its neighbours. If any neighbouring bead is also crystalline, it is counted as the second bead of the same cluster. Similarly, we move recursively from neighbour to neighbour to compute the cluster size. If a bead does not have any new crystalline neighbours, then we move to the next bead to identify the second cluster in the system and so on. At the end, all cluster sizes are compared and the largest cluster is identified.

We note here that, in our simulations, whenever a nucleus that is significantly bigger than the critical nucleus (as define later) is seen, this always develops into a large crystalline structure.

2.2.2 Nematic order parameter

As suggested by Nicholson and Rutledge[16], we used the Kuhn step nematic order parameter $P_{2,K}$ to measure the flow-induced alignment of chains. We split the chains into Kuhn segments, each Kuhn segment (denote as K_L) consists of 12 consecutive beads along the chain for this polyethylene model[16] and $P_{2,K}$ is the largest eigenvalue of

$$Q_{\alpha\beta} = \frac{1}{N_K} \sum_{j=1}^{N_K} \left(\frac{3}{2} \hat{u}_{j\alpha} \hat{u}_{j\beta} - \frac{1}{2} \delta_{\alpha\beta} \right), \quad (6)$$

where N_K is the number of Kuhn segments in the system, $\hat{u}_j$ is the unit vector parallel to the end-to-end vector of Kuhn segment j, δ is the Kronecker delta and $\alpha, \beta = x, y, z$.[39]. This order parameter is close to unity when all chains are parallel to each other and close to zero when all chains are oriented randomly.

2.3 Simulation details

We have performed molecular dynamics simulations of mono-disperse and binary mixtures of linear polymer chains to study nucleation under shear flow. The mono-disperse system consists of 300 chains of length 1000 beads and the binary blends consists of longer chains of length 1000 beads, while the lengths of shorter chains were varied from 500 to 125 bead in different simulations. We denote mono-disperse system as “M_1K” and binary systems with 50% chains of length 500 beads, 50% chains of length 250 beads and 50% chains of length 125 beads as “B_50-500”, “B_50-250” and “B_50-125” respectively. We provide complete information for these systems in table 2. We also denote the total number of beads, long chain beads and short chains beads in the system as M, M_L and M_S respectively.

Table 2 Details of simulated systems.

System	N	#N_L	#N_S	%M_L	%M_S
M_1K	300000	300	-	100	-
B_50-500	300000	150	300	50	50
B_50-250	300000	150	600	50	50
B_50-125	300000	150	1200	50	50

We performed all shear simulations under constant volume and constant temperature conditions. The use of NVT for these crystallisation simulations is appropriate as, for this study, we focus on nucleation, which is a local process and the critical nucleus size is very small compared to the whole system. Hence densification due to crystallisation has a negligible effect on the overall system for nuclei around the critical size. The shear flow was generated via Lees Edwards boundary conditions[40] and the DPD thermostat[41]. This protocol has been used previously to study polymer crystallisation under flow[17,22]. We used the friction coefficient for the thermostat to be 0.5 τ^{-1} and the cut-off radius to be $R_c = 1.3\sigma$, where $\tau = \sqrt{\frac{m\sigma^2}{k_B T}}$ and m is the mass of the bead, k_B is the Boltzmann constant, T is the temperature in Kelvin and σ is the size of the beads. The integration timestep used in the simulations at 380K was 0.0069τ, which in real units is 5.84 femtoseconds. We used the ESPResSo[42] molecular dynamics package for all simulations.

2.4 Equilibration

To produce equilibrated binary blends, we began with an equilibrated system of 300 monodisperse chains of 1000 beads (C1000) from our previous work[22]. We cut 150 of the chains at the centre and simulated in NVT at 550K until the short chains diffused through their radius of gyration. We then cut all short chains again and reequilibrated as before, then repeated this process one further time. This produced a series of binary blends of 150 long chains of 1000 beads blended at a monomer fraction of 0.5 with short chains of length 500, 250 and 125 monomers, all equilibrated at 550K. The blend with short chains of 125 monomers has the widest possible separation of molecular weights, while the short chains remain entangled, and we expect to see the strongest long chain enrichment in this system. We then maintained a temperature of 550K, but changed the density to that of the desired crystallisation temperature, Tc, (380K) at 1 atm and ran a short NVT simulation to allow this density change to relax. Finally we quenched to T_c to produce a fully relaxed system at T_c with the correct density.

2.5 Start-up shear flow

After the quench to T_c we imposed a continuous start-up shear at a rate $\dot{\gamma}$ and ran the simulation until the entire box crystallised. We ran these shear simulations at three different shear rates, $\dot{\gamma} = 7\times10^7$, 13.1×10^7 and 24.8×10^7 1/sec. The Rouse time for the C1000 chains at 380K, obtained from analysis of direct non-linear shear simulations and time-temperature superposition results[22], is 155.2 ns. Thus the Rouse Weissenberg numbers $\mathrm{W_{iR}} = \dot{\gamma}\tau_{RL}$, where τ_{RL} is the long chain Rouse time, for our chosen shear rates are 10.9, 20.3 and 38.5. The Rouse Weissenberg numbers for each chain length are shown in table 3. To sample the nucleation statistics, we ran 4-8 repeats of this start-up shear flow for each shear rate and each blend in table 2.

Table 3 Rouse Weissenberg numbers at 380K, from Rouse scaling of the C1000 τ_R, for each shear rate and chain length in our study.

$\dot{\gamma}$ [1/sec]	$\dot{\gamma}\tau_R$ C1000	$\dot{\gamma}\tau_R$ C500	$\dot{\gamma}\tau_R$ C250	$\dot{\gamma}\tau_R$ C125
7×10^7	10.9	2.725	0.681	0.170
13.1×10^7	20.3	5.08	1.27	0.317
24.8×10^7	38.5	9.63	2.41	0.602

2.6 Simulation analysis techniques

Below we describe a series of techniques to extract useful nucleation information from our simulation trajectories.

2.6.1 Nucleus induction time

In molecular dynamics simulations of the nucleation process, estimation of the induction time is an important task. In order to estimate the induction times, we used the crystallinity order parameter, as described in section 2.2, to identify the largest cluster in the system for all trajectories and performed a mean first passage time (MFPT) analysis[43] to estimate the induction time for nucleation. This approach is based on classical nucleation theory to find the induction time. The mean first passage time analysis is performed on the evolution of the largest cluster in the system to define the average time of the first appearance of a cluster with size n_{max}:

$$\tau(n_{max}) = \frac{1}{M}\sum_{i=1}^{M}\tau_{n_{max}}^{(i)}, \tag{7}$$

where M is the total number of trajectories and $\tau_{n_{max}}^{(i)}$ is the time when a cluster with size n_{max} first appears. As nucleation is followed by fast cluster growth, $\tau(n_{max})$ has a sigmoidal shape and can be fitted by the equation:

$$\tau(n_{max}) = 0.5\tau^*[1+\mathrm{erf}(Z\sqrt{\pi}(n_{max}-n^*))], \tag{8}$$

where τ^* is the induction time, n* is the critical nucleus size, Z is the Zeldovich factor and the error function is $\mathrm{erf} = \frac{2}{\sqrt{\pi}}\int_0^x e^{-x^2}dx$. This mean first passage time has been successfully used for this purpose in many recent studies[17,22,33–36]. Equation (8) captures the MFPT data from our simulations well. Figure 1 shows the fits for two representative simulations involving different blends and shear rates.

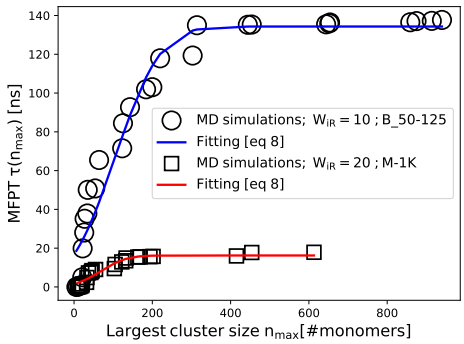

Fig. 1 Comparison of the mean first passage time (MFPT) data from simulations with fitting from equation (8), for two representative simulations involving different blends and shear rates.

2.6.2 Nucleus composition

We also developed a histogram method to efficiently extract good statistical resolution of the nucleus composition from our MD trajectories during a transient start-up flow. We extracted this composition data, as follows. We saved configurations every 20,000 timesteps and separated these by accumulated strain, γ, into windows of 0.5 strain units. For each configuration we identified the largest 7 separate clusters using the crystallinity order parameter. For each strain window we binned all identified clusters by total cluster size, N_T, into bins of width 20 monomers. We rejected any bin with fewer than 10 clusters. Within each strain-N_T bin we computed the monomer fraction of clusters by summing over long chain monomers in all clusters and dividing by the total monomers summed over all clusters. This approach captures data from all clusters, not just those that successfully nucleate. We then repeated this analysis over only successful nuclei. To define a successful nucleus, we began with a cluster of 500 monomers and traced these back in time. Moving backwards to the previous snapshot, we identified the successful cluster as the cluster that contains the largest number of the original 500 monomers. We continue to track backwards until the cluster has less than 10 monomers. We then repeated the above analysis, but considering only successful clusters. Beyond a cluster size of 200 monomers the data for 'all' and 'successful' nuclei are identical so we omit the data for 'all' clusters. Finally, we repeated this whole analysis of nucleus composition, but replacing sums over monomers with sums over chain stems in the nucleus. This provides a map for the chain composition of growing nuclei.

3 The polySTRAND model

The polySTRAND model is a nearly analytic continuum model of flow-induced nucleation in polymers. It was derived[24] via systematic multiscale modelling, involving the coordinated use of MD from monodisperse chains[16], highly coarse-grained kinetic Monte Carlo simulations of polydisperse chains[25,26] and thermodynamic modelling to produce a low-dimensional projection of the nucleation problem[24,27,28]. The kinetic Monte-Carlo algorithm used in the derivation of the polySTRAND model is the

Graham and Olmsted (GO) model[25,26]. The model predicts that stems and monomers from long chains are enriched for nucleus sizes around and below the critical nucleus.

In the derivation of the polySTRAND model, only MD data on monodisperse polymers was used. Such data clearly produce no information about long chain enhancement. Thus long chain enhancement arises naturally from generalising the model to polydisperse systems. The polySTRAND model makes assumptions about the nucleus structure and these determine the quantitative details of the long chain enhancement. Our MD data test these assumptions both qualitatively and quantitatively.

3.1 Model summary

Throughout this article we use the GO-polySTRAND[24] variant of this model, which agrees closely with kinetic Monte Carlo simulations[25,26,29] that implement the physics described below. The polySTRAND model considers nuclei to be ellipsoids of N_S stems and N_T monomers. For a given N_S and N_T, the quiescent nucleus potential comprises a bulk energy gain proportional to the nucleus size, N_T, and a surface area cost proportional to the surface area, S. Hence the potential is $U_{\text{nuc}} = -\varepsilon_B N_T + \mu_S S(N_T, N_S)$, where ε_B is the free energy of crystallisation per monomer, μ_S is the surface energy cost, with all energies in units of $k_B T$. Flow is imposed by subtracting the flow-induced entropic changes due to the Kuhn step nematic order ($P_{2,K}$) from the entropy penalty for crystallisation, which is implicitly contained in ε_B. Under flow, each chain length acquires a different nematic order and so has a distinct attachment rate. Thus, the stem attachment k_{st}^+ and detachment k_{st}^- rates have the ratio $k_{st}^+/k_{st}^- = \phi_i \exp(-\Delta U_{\text{nuc}} + \Gamma P_{2,Ki})$, where ϕ_i and $P_{2,Ki}$ are the melt monomer fraction and Kuhn step nematic order, respectively, of species i and Γ is a dimensionless order-one model parameter, linking nematic order to reduction in entropy penalty. A Γ value of one means that changing the nematic order of a Kuhn step from isotropic to fully aligned leads to an entropy loss of $k_B T$. Stems comprise of crystallised segments of a single chain and existing stems attach or detach monomers along the same chain, whose volume fraction at the nucleus surface is taken to be 1. Thus the ratio of rates for existing stems is identical to k_{st}^+/k_{st}^- but with $\phi_i = 1$. The polySTRAND model provides an analytic expression for the nucleus free energy, $F(\{w_i\},\{v_i\},N_T,N_s)$, where w_i and v_i are the stem and monomer fractions, respectively. This free energy is minimised over $\{w_i\},\{v_i\}$ and N_s, subject to the constraints $\sum_i w_i = 1$ and $\sum_i v_i = 1$, which are imposed via Lagrange multipliers. This minimisation can be performed nearly analytically and requires the numerical solution of only a single non-linear equation. Thus, taking $q = N_s/N_T$, the free energy of a nucleus is given by

$$\begin{aligned} F(N_T,N_s) = N_T \sum_i \big[& q w_i (2\log w_i - \log\phi_i) - v_i \log v_i \\ & + (v_i - q w_i)\log(v_i - q w_i) - (\Gamma P_{2,Ki}) v_i \big] \\ & + N_S \log q - \varepsilon_B N_T + \mu_S S(N_T,N_S), \end{aligned} \tag{9}$$

where all free energies are given in units of $k_B T$. Minimisation over $\{w_i, v_i\}$ with $\sum_i w_i = \sum_i v_i = 1$ yields the optimised stem and monomer fractions,

$$w_i = B\phi_i \frac{\exp(\Gamma P_{2,Ki})}{1 - A\exp(\Gamma P_{2,Ki})},\ v_i = B\phi_i q \frac{\exp(\Gamma P_{2,Ki})}{\big[1 - A\exp(\Gamma P_{2,Ki})\big]^2}, \tag{10}$$

where A and B are Lagrange multipliers, determined by,

$$\sum_i \frac{q\phi_i \exp(\Gamma P_{2,Ki})}{\big(1 - A\exp(\Gamma P_{2,Ki})\big)^2} = \sum_i \frac{\phi_i \exp(\Gamma P_{2,Ki})}{1 - A\exp(\Gamma P_{2,Ki})}, \tag{11}$$

and

$$B = \left(\sum_i \frac{\phi_i \exp(\Gamma P_{2,Ki})}{1 - A\exp(\Gamma P_{2,Ki})} \right)^{-1} \tag{12}$$

Here, equation (11) is solved numerically for A and equation (12) provides B directly. See ref[24] for full mathematical details. In equation (10) the fraction of stems of species i in the nucleus is enhanced by a factor of $\frac{\exp(\Gamma P_{2,Ki})}{1 - A\exp(\Gamma P_{2,Ki})}$, while the fraction of monomers is enhanced by a further factor of $1 - A\exp(\Gamma P_{2,Ki})$ in the denominator. As long chains are the most readily deformed under flow, the polySTRAND model predicts enrichment of long-chain stems and further enrichment of monomers from long chains. Hence the model predicts that long-chain stems are enriched relative to the melt monomer distribution and that these stems are longer than average. This predicted nucleus structure is seen directly in our MD simulations (see section 4.2).

3.2 Nucleation composition and barrier under flow

The nucleation barrier under flow can be calculated from the polySTRAND model as follows. For specified values of N_T,N_s, $\{\phi_i\}$ and $\{P_{2,Ki}\}$, the normalisation constants A and B can be found by numerical solution of equation (11) and direct substitution into equation (12). The values of A and B then provide the chain and monomer fractions, $\{v_i\}$ and $\{w_i\}$, via equation (10). Substitution of these fractions into equation (9) provides the 2-dimensional barrier $F(N_T,N_s)$. This 2D barrier is projected onto a single coordinate, N_T, as follows. For a given N_T, numerical minimisation of $F(N_T,N_S)$ over N_S gives N_S^*, the optimum number of strands. Leading order fluctuations about N_S^* are included via

$$F_{\text{pS}}(N_T) = F(N_T,N_S^*) + \ln\left(\frac{1}{2\pi} \frac{\partial^2 F}{\partial N_S^2}\bigg|_{N_S = N_S^*} \right), \tag{13}$$

where $\frac{\partial^2 F}{\partial N_S^2}$ is computed via the standard central difference expression and where $F_{\text{pS}}(N_T)$ denotes the 1D polySTRAND barrier with N_s fluctuations. The same method computes F_{pS}^{q}, the polySTRAND barrier for quiescent chains. Finally, subtracting the change in the barrier due to chain deformation, $F_{\text{pS}}^{\text{q}} - F_{\text{pS}}$, from a full calculation of the quiescent GO model barrier, F_{GO}^{q}[26] provides the overall nucleation barrier,

$$F_{\text{final}}(N_T) = F_{\text{GO}}^{\text{q}}(N_T) - \Big(F_{\text{pS}}^{\text{q}}(N_T) - F_{\text{pS}}(N_T) \Big), \tag{14}$$

The quiescent GO model barrier can be readily and cheaply computed from the nearly analytic algorithm in Appendix A of Jolley and Graham[29]. Read *et al.*[24] showed that, by this method, the polySTRAND model captures very closely the nucleation barrier

in the GO model[25], obtained by direct Monte Carlo simulation[29]. We then search numerically over N_T to find the barrier peak F^*.

The calculation above provides the nucleus composition, namely the monomer and chain fractions, at the N_S^* corresponding to each N_T. This composition varies only weakly with N_s about N_S^* so we compute the composition at N_S^* and neglect the weak effect of fluctuations about N_S^* on the composition. This calculation provides the nucleus monomer and chain fraction at each value of N_T.

3.3 Modelling the induction time during a start-up flow

Our MD simulations are performed in start-up flow where the nematic order P_{2K} evolves transiently. This means that the nucleation rate begins at the quiescent value and grows as the chain deformation increases. Hence the extracted induction time is the average over a dynamically increasing nucleation rate. Here we describe how to calculate the corresponding quantity in the polySTRAND model.

We write the nucleation rate per simulation box as $\dot{N}(t) = \dot{N}_0\xi(t)$, where $\dot{N}_0$ is the quiescent nucleation rate per simulation box and $\xi(t)$ is the ratio of the flow induced and quiescent nucleation rates. The nucleation rate per simulation box is the product of the quiescent nucleation rate per unit volume, $\dot{N}_q$, and the simulation box volume V. Thus the probability, $S(t)$, that the simulation box has survived (ie not nucleated) at t obeys the differential equation

$$\frac{\mathrm{d}S}{\mathrm{d}t} = -\dot{N}_0\xi(t)S(t). \tag{15}$$

This equation has the solution

$$S(t) = \exp\left(-\int_0^t \dot{N}_0\xi(t')\mathrm{d}t'\right). \tag{16}$$

As the probability density, $P(t)$, of a nucleation event at time t is given by $P(t) = -\frac{\mathrm{d}S}{\mathrm{d}t}$, we have $P(t) = \dot{N}_0\xi(t)S(t)$ (from equation (15)). Substituting this expression into the expectation integral for the induction time and using equation (16) gives

$$\begin{aligned} <\tau> &= \int_0^\infty tP(t)\mathrm{d}t \\ &= \int_0^\infty t\dot{N}_0\xi(t)\exp\left(-\int_0^t \dot{N}_0\xi(t')\mathrm{d}t'\right)\mathrm{d}t \end{aligned} \tag{17}$$

In the polySTRAND model the ratio of nucleation rates, $\xi(t)$, is dominated by the Boltzmann factor of the change in barrier height[24,28], hence $\xi(t) = \exp(F_q^* - F_\Lambda^*(t))$, where F_q^* and $F_\Lambda^*(t)$ are the quiescent and flow-induced nucleation barriers, respectively. Both barriers can be calculated by the method in section 3.2. For this calculation we take $P_{2,K}$ for the short and long chains from a series of simulation snapshots, using the process in section 2.2.2. This allows $F_\Lambda^*(\{P_{2,K}\})$ to be computed at a set of discrete time points, which can be used to numerically evaluate the integrals in equation (17) to provide the induction time for each blend and flow rate.

3.4 Determining parameters to compare with simulations

To compare to our simulations, the polySTRAND model requires 3 barrier parameters (Γ, ε_B and μ_s), to compute the nucleation barrier and degree of long-chain enrichment, along with an additional kinetic parameter $\dot{N}_0$ required to compute the induction time. We can obtain the barrier parameters from independent quiescent simulations alone. However, the single kinetic parameter must be obtained from our FIC simulations, as detailed below. Usually the polySTRAND model requires further parameters to compute $P_{2,Ki}$ under flow and the crystallisation growth kinetics. However, here MD provides $P_{2,Ki}$ and computing the enrichment and induction time does not require the growth kinetics.

3.4.1 Barrier parameters

In the polySTRAND model, the parameters ε_B and μ_s determine the quiescent nucleation barrier. The corresponding quiescent barrier for our MD system was determined by Yi *et al.*[35] via survival probability analysis and classical nucleation theory. We used their projection formulae to obtain the quiescent barrier height, ΔF^*, and the critical nucleus size, n^* and matched these in the polySTRAND model by adjusting ε_B and μ_s, obtaining -0.1459 and 0.89 respectively. We took the default value of $\Gamma = 1$ and extracted the nematic order for each chain length, $P_{2,KL/S}$, directly from MD, using equation (6).

3.4.2 Kinetic parameter

The single kinetic parameter is the nucleation rate per simulation box $\dot{N}_0$. We cannot obtain this from quiescent simulation as direct MD simulations of quiescent nucleation at 380K are not computationally feasible. Instead we obtained $\dot{N}_0$ by fitting equation (17) to a limited subset of MD data, in which there is no long chain enhancement. Specifically, we used our simulated induction times for the systems M_1K, B_50-500 and B_50-250, at $W_{iR} = 38.5$. At this high shear rate these three blends have nearly the same induction time in both the simulations and the model (see figure 2), thus we balanced the fit across these three blends to obtain the value $\dot{N}_0 = 5.4 \times 10^{-79}$ ns^{-1}. We emphasize that only a limited amount of induction time data was used in fitting this parameter and that no long chain enhancement occurred in these fitted data.

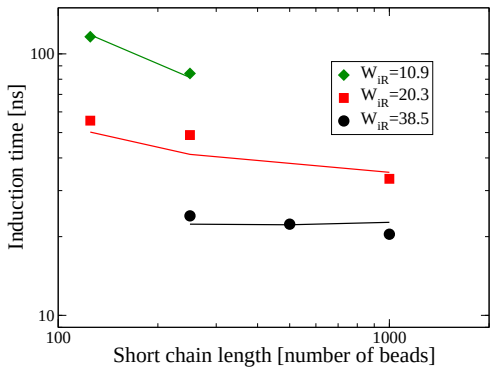

Fig. 2 Induction time for 50:50 PE blends at 380K with long chains of 1000 beads. Both the short chain length and shear rate vary. Points are MD simulation results and lines are results from the polySTRAND model. The simulation results for M_1K are from ref[22].

4 Simulation results and comparison with the polySTRAND model

4.1 Induction time

We extracted induction times from our MD simulations, using the methods in section 2.6.1, and these are plotted in figure 2. This figure shows how the induction time varies with both flow rate and blend composition. In this plot the long chain length is 1000 beads in all cases, whereas the short chain length varies between 1000 (monodisperse) and 125 beads (see table 2). At the highest shear rate, $W_{iR} = 38.5$, there is only a very weak variation of the induction time with blend composition. At this shear rate all three molecular weights (C1000, C500 and C125) are at a Rouse Weissenberg number exceeding one (see table 3) hence all chains deform similarly during the initial part of the shear transient. Since nucleation occurs during this early part of the transient then the induction time is independent of polydispersity for these three simulations. We note that as the shear rate lowers, differences in induction time between the blends emerge and grow. At $W_{iR} = 20.3$ the induction time begins to rise with decreasing short chain length and this effect is stronger still at $W_{iR} = 10.9$. This suggests that as the shear rate reduces there is a greater separation in deformation between the short and long chains.

Figure 2 also shows the calculated induction times from the polySTRAND model, using the calculation method in section 3.2 and the parameters in section 3.4. The variation of the induction time with both shear and blend composition is captured quantitatively by the polySTRAND model. All parameters are determined from independent quiescent simulations, apart from $\dot{N}_0$, which is fitted to the $W_{iR} = 38.5$ data alone.

4.2 Long chain enrichment

We extracted the degree of long chain enrichment from our MD simulations using the methods in section 3.4. For the blends B_50-500 and B_50-250, we did not see any significant long-chain enrichment at any of the 3 shear rates. However for the most widely separated blend (B_50-125) we saw significant long chain enrichment at both shear rates. These results are shown in figures 3 and 4. For the monomer fraction, at lower strains (fig. 3(a-c)) the nucleus composition matches the melt composition. However, at larger strains, where the difference in chain deformation between the two species is more pronounced, a difference in the nucleus monomer fraction and the melt fraction emerges and grows systematically (fig. 3)(d-j). A similar picture is seen for the chain fraction in figure 4. Again the chain fraction matches the melt monomer composition at low strains but begins to deviate at larger strains as the differences in chain deformation become more pronounced. The chain fraction is less widely separated than the monomer fraction. Thus our simulations show that long-chain stems are enriched in nuclei and there is an even greater enrichment of monomers from long chains. Consequently, these long-chain stems are typically longer than the average stem length. This leads to a specific nucleus structure which is exemplified in the nucleus snapshot shown in figure 5. This nucleus has a core of elongated long chain stems (red), while the short-chain stems (grey) are fewer and shorter and these tend to plug the gaps around the long-chain stem core. These results provide clear evidence in MD of the enrichment of long chains as predicted by the polySTRAND model[24].

We now compare the calculations of the polySTRAND model with the long-chain enrichment extracted from our MD simulations. For this comparison all parameter are obtained from independent quiescent simulations (see section 3.4.1). The polySTRAND calculations for B_50-125, for each strain window, at $W_{iR} = 10.9$ are plotted in figures 3 and 4, where strain windows of width 1 were used. The model captures the simulation data well for both $\{v_i\}$ and $\{w_i\}$. Both the data and model show a constant composition for each window, independent of nucleus size, N_T. Thus, we can extract a single composition value from each strain window by averaging over each N_T for which there is simulation data. The resulting average composition separations for monomers, $v_L - v_S$, and stems, $w_L - w_S$, are plotted against nematic order difference, $P_{2,KL} - P_{2,KS}$, in figure 6 for both shear rates. The model quantitatively captures all of these simulation results, from independently determined parameters. Furthermore, the model predicts that different shear rates collapse to a mastercurve and the simulations are consistent with this. The polySTRAND model also correctly predicts no significant long-chain enrichment for the other blends in this study (B_50-500 and B_50-250). The model parameters that capture the long-chain enrichment, simultaneously capture the induction time data (see figure 2).

In this work, the MD data are well-described with a value of $\Gamma = 1$, where this parameter connects the change in nematic order of a Kuhn segment to entropy loss. In our previous work[24], we obtained values of this parameter for a set of MD simulations and two experimental systems. Fitting to nucleation rate data from MD simulations of monodisperse C150 PE chains[16] gives $\Gamma = 0.65$. By fitting to FIC experiments on isotactic polypropylene and isotactic poly-1-butene, we found Γ values of 4.3 and 1.3 respectively. Thus, there is some evidence that Γ depends weakly on the chemical structure of the polymer chains. The small difference in Γ required to describe the MD data from reference[16] and our data herein may be due either to uncertainties in the quiescent barrier or due to differences in the density of chain ends arising from the large differences in polydispersity between the two simulation set-ups.

5 Conclusions

In conclusion, we ran MD simulations of bimodal blends of linear polyethylene under flow and tracked crystal nucleation. In these simulations we observed directly that nuclei are enriched with long chains, as predicted by the polySTRAND model[24]. Furthermore in MD this enrichment is independent of nucleus size, up to and just beyond the critical nucleus size and the enrichment data from two different shear rates collapse onto a mastercurve of composition against nematic order difference between the short and long chains. In both the simulations and the model, long chain stems are enriched and there is a further enrichment of long chain monomers. Consequently, the nucleus structure in MD comprises a core of elongated long chain stems, with the rarer

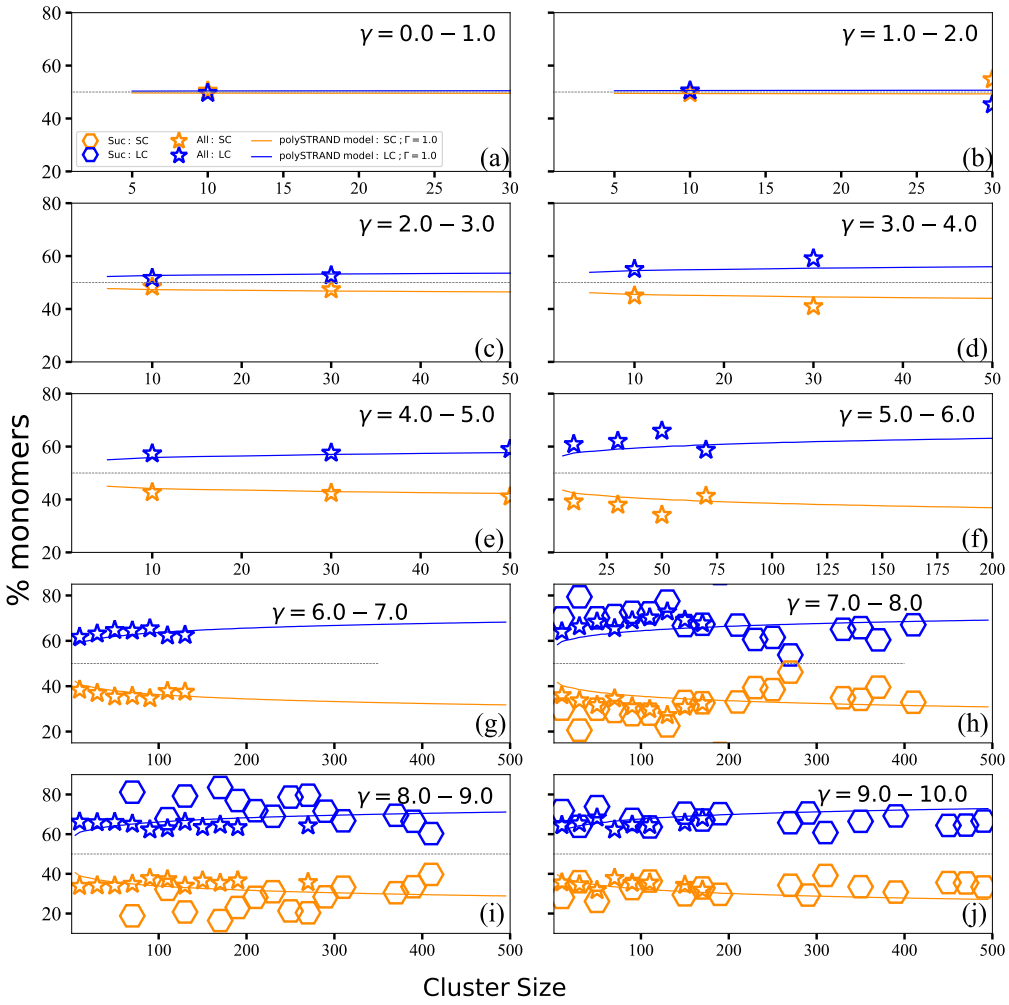

Fig. 3 Nucleus monomer distribution for our bimodal blend, B_50-125, at 380 K (a-j) during a start-up shear flow at $W_{iR} = 10.9$. The upper (blue) and lower (orange) symbols correspond to monomers from long and short chains, respectively. Stars correspond to all observed clusters, while hexagons correspond to data only from clusters that successfully nucleate. The lines are results from the polySTRAND model[24] (see the main text for details). Here γ is the shear strain, SC/LC refers to short/long chains, Suc means only successful nuclei, All means all observed nuclei and Γ is a parameter of the polySTRAND model.

and shorter short-chain stems plugging the gaps around this long-chain stem core (see figure 5). Our results show that the key role of nematic order, identified from nucleation simulations of monodisperse chains[16], extends to polydisperse systems. There is prior indirect evidence of this long chain enrichment from the super-exponential behaviour of the nucleation rate in shear experiments and from the polySTRAND model. However, our MD simulations provide a direct quantification of this effect. This combination of experiments, simulation and modelling constitutes strong evidence for the importance of long chain enrichment in the flow-induced nucleation mechanism.

The polySTRAND model[24] makes assumptions about the nucleus structure. Specifically, that chains within the nucleus are arranged into stems and each stem contains a single chain. These assumptions determine the quantitative degree of long chain enhancement and lead to specific predictions about the long-chain enhancement, which were tested by our MD data. The most significant prediction is that the fraction of both long chain stems and monomers are enriched, with monomers being more enriched than stems. The polySTRAND model quantitatively captures the degree of long chain monomer and stem enrichment in our simulations. This comparison required only a small number of free parameters, which we obtained from a minimal subset of the induction time data in which long chain enhancement was absent. The same model parameters also correctly capture the nucleus induction time seen in our simulations, for all four blends at a range of shear rates. The qualitative and quantitative success of the polySTRAND model in capturing details of the nucleation seen in our MD simulations supports the validity of the physical assumptions made in deriving this model.

There is a developing body of evidence supporting the role of nematic precursors in polymer nucleation[13,44–50], particularly under flow. Although, investigating nematic precursors was not an aim of this study, we can draw some conclusions from our re-

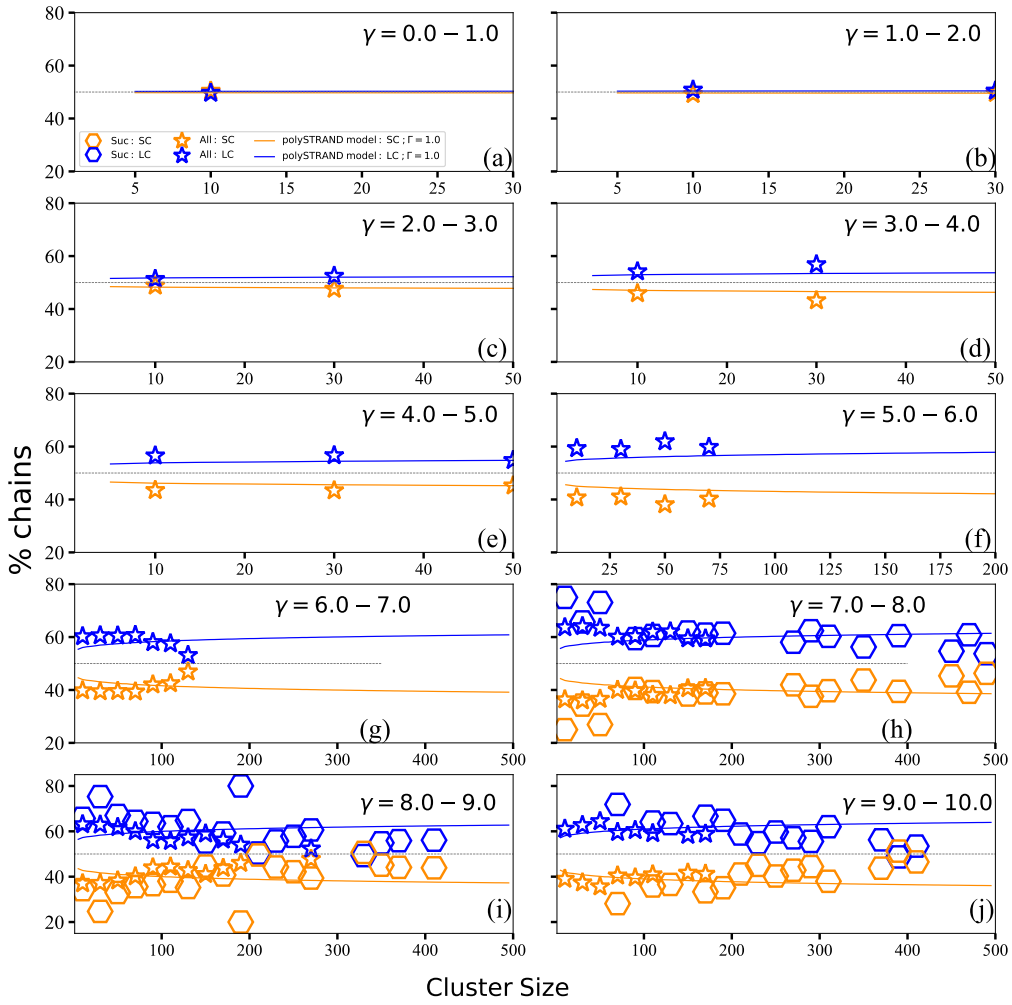

Fig. 4 Nucleus chain distribution for our bimodal blend, B_50-125, at 380 K (a-j) during a start-up shear flow at $W_{iR} = 10.9$. The legend is the same as figure 3.

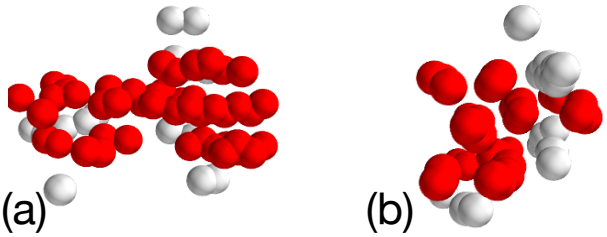

Fig. 5 Simulation snapshot showing the typical nucleus structure from blend B_50-125, for a nucleus of 66 monomers at $W_{iR} = 20$ and a shear strain of 6.45. Only crystallised monomers are shown and long and short chain monomers are coloured red and grey, respectively. The viewing directions are perpendicular (a) and parallel (b) to the nucleus stem axis.

sults. First, the polySTRAND model tracks the arrangement of monomers within oriented strands inside the nucleus, but not the ordering of these strands within the nucleus. This level of description is consistent with nucleation into a nematic precursor. Second, our results show that nematic order is the key order-parameter controlling the induction time (figure 2) and nucleus composition (figure 6), which is also consistent with nucleation into a nematic precursor. We cannot make a definitive statement at this stage and further work is needed, with MD positioned to play a useful role. Chain stiffness is likely to promote nematic phases, as in experiments on PEEK[18,47,50], and stiffness can readily be controlled in MD simulations by adjusting the bonded interactions in the forcefield.

Long-chain enrichment is central to the structure of flow-induced nuclei from polydisperse systems and this long-chain enrichment must be captured to correctly predict the nucleation rate. Evidence across experiments, simulations and modelling shows that polydispersity plays a central role in flow-induced nucleation as multiple chain lengths co-operate in nontrivial ways to compose the growing nucleus. Experiments and simulations across several chemistries (polyethylene, polypropylene[10] and isotactic poly-1-butene[51]) can all be described by the same model. This is strongly suggestive of universal behaviour in polymer FIC that transcends the chemical composition of the chains. This is supported by experimental evidence of the universal role

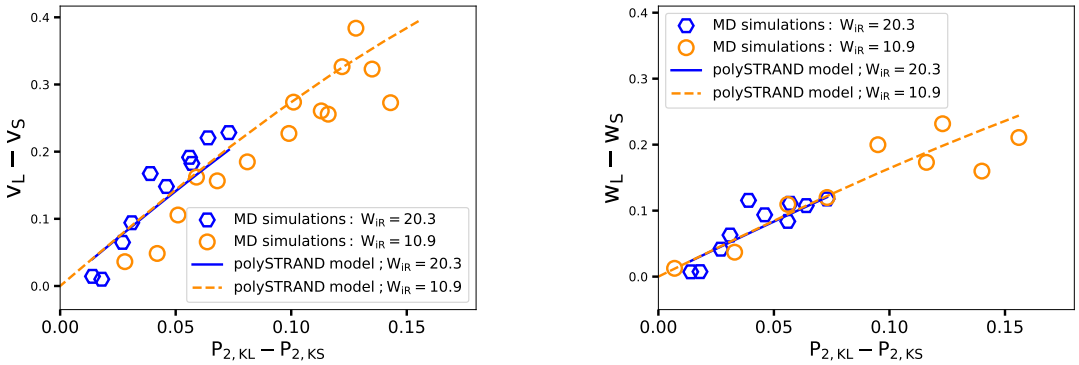

Fig. 6 The difference in nucleus composition between long and short chains, for blend B_50-125, against the difference in nematic order parameter for monomer fraction (a) and stem (chain) fraction (b). Comparison of MD simulations at 380K with the polySTRAND model[24].

of critical mechanical work in determining the nucleation density and onset of shish kebab structures across many different polymer chemistries[5,6,52,53]. We conclude that, polydispersity has a central role in the mechanism of flow-induced nucleation. As the polySTRAND model[24] predicts this effect quantitatively it provides a tool for the control of FIC by tailoring the molecular weight distribution and processing conditions.

Conflicts of interest

There are no conflicts to declare.

Acknowledgements

We thank Daniel Read, Oliver Harlen and Chinmay Das for useful discussions about MD simulations under shear. We acknowledge funding from the EPSRC (grant No. EP/P005403/1) and access to the University of Nottingham High Performance Computing and HPC Midlands+ (EPSRC grant No. EP/P020232/1).

Notes and references

1 A. Keller and H. Kolnaar, in *Processing of Polymers*, ed. H. Meijer, Wiley-VCH, Weinheim, 1997, vol. 18, p. 189.
2 F. L. Binsbergen, *Nature*, 1966, **211**, 516–517.
3 G. Kumaraswamy, A. M. Issaian and J. A. Kornfield, *Macromolecules*, 1999, **32**, 7537–7547.
4 M. Seki, D. W. Thurman, J. P. Oberhauser and J. A. Kornfield, *Macromolecules*, 2002, **35**, 2583–2594.
5 H. Janeschitz-Kriegl, E. Ratajski and M. Stadlbauer, *Rheologica Acta*, 2003, **42**, 355–364.
6 O. O. Mykhaylyk, P. Chambon, R. S. Graham, J. P. A. Fairclough, P. D. Olmsted and A. J. Ryan, *Macromolecules*, 2008, **41**, 1901–1904.
7 S. Kimata, T. Sakurai, Y. Nozue, T. Kasahara, N. Yamaguchi, T. Karino, M. Shibayama and J. A. Kornfield, *Science*, 2007, **316**, 1014–1017.
8 M. Stadlbauer, H. Janeschitz-Kriegl, G. Eder and E. Ratajski, *J. Rheol.*, 2004, **48**, 631–639.
9 E. E. B. White, H. H. Winter and J. P. Rothstein, *Rheol Acta*, 2012, **51**, 303–314.
10 R. Pantani, I. Coccorullo, V. Volpe and G. Titomanlio, *Macromolecules*, 2010, **43**, 9030–9038.
11 F. G. Hamad, R. H. Colby and S. T. Milner, *Macromolecules*, 2015, **48**, 3725–3738.
12 Z. Wang, J. Ju, J. Yang, Z. Ma, D. Liu, K. Cui, H. Yang, J. Chang, N. Huang and L. Li, *Sci Rep*, 2016, **6**, 32968.
13 K. Cui, Z. Ma, N. Tian, F. Su, D. Liu and L. Li, *Chem. Rev.*, 2018, **118**, 1840–1886.
14 R. S. Graham, *J Rheol*, 2019, **63**, 203–214.
15 D. A. Nicholson and G. C. Rutledge, *The Journal of Chemical Physics*, 2016, **145**, 244903.
16 D. A. Nicholson and G. C. Rutledge, *Journal of Rheology*, 2019, **63**, 465–475.
17 M. Anwar, J. T. Berryman and T. Schilling, *The Journal of Chemical Physics*, 2014, **141**, 124910.
18 J. Seo, A. M. Gohn, R. P. Schaake, D. Parisi, A. M. Rhoades and R. H. Colby, *Macromolecules*, 2020, **53**, 3472–3481.
19 J. D. Hoffman and J. I. Lauritzen, *J. Res. Natl. Bur. Stand. Sect. A*, 1961, **65A**, 297–336.
20 M. Anwar and R. S. Graham, *Journal of Polymer Science Part B: Polymer Physics*, 2019, **57**, 1692–1704.
21 C. McIlroy and R. S. Graham, *Additive Manufacturing*, 2018, **24**, 323.
22 M. Anwar and R. S. Graham, *J. Chem. Phys.*, 2019, **150**, 084905.
23 K. W. Hall, T. W. Sirk, S. Percec, M. L. Klein and W. Shinoda, *The Journal of Chemical Physics*, 2019, **151**, 144901.
24 D. J. Read, C. McIlroy, C. Das, O. G. Harlen and R. S. Graham, *Phys. Rev. Lett.*, 2020, **124**, 147802.
25 R. S. Graham and P. D. Olmsted, *Phys. Rev. Lett.*, 2009, **103**, 115702.
26 R. S. Graham and P. D. Olmsted, *Faraday Discussions*, 2010, **144**, 71–92.
27 M. J. Hamer, J. A. Wattis and R. S. Graham, *Journal of Non-Newtonian Fluid Mechanics*, 2010, **165**, 1294 – 1301.
28 M. J. Hamer, J. A. D. Wattis and R. S. Graham, *Soft Matter*, 2012, **8**, 11396–11408.

29 K. Jolley and R. S. Graham, *Rheologica Acta*, 2013, **52**, 271–286.

30 W. Paul, D. Y. Yoon and G. D. Smith, *The Journal of Chemical Physics*, 1995, **103**, 1702–1709.

31 N. Waheed, M. S. Lavine and G. C. Rutledge, *The Journal of Chemical Physics*, 2002, **116**, 2301–2309.

32 N. Waheed, M. Ko and G. Rutledge, *Polymer*, 2005, **46**, 8689–8702.

33 P. Yi and G. C. Rutledge, *The Journal of Chemical Physics*, 2009, **131**, 1–12.

34 P. Yi and G. C. Rutledge, *The Journal of Chemical Physics*, 2011, **135**, 11.

35 P. Yi, C. R. Locker and G. C. Rutledge, *Macromolecules*, 2013, **46**, 4723–4733.

36 M. Anwar, F. Turci and T. Schilling, *The Journal of Chemical Physics*, 2013, **139**, 214904.

37 M. Anwar and T. Schilling, *Polymer*, 2015, **76**, 307 – 312.

38 N. Waheed, M. Ko and G. Rutledge, *Polymer*, 2005, **46**, 8689 – 8702.

39 P. G. de Gennes and J. Prost, *The Physics of Liquid Crystals*, Oxford University Press, 1995.

40 A. W. Lees and S. F. Edwards, *Journal of Physics C: Solid State Physics Volume 5 Number 15*, 1972, **5**, 1921–1929.

41 T. Soddemann, B. Dünweg and K. Kremer, *Phys. Rev. E*, 2003, **68**, 046702.

42 H. J. Limbach, A. Arnold, B. A. Mann and C. Holm, *Computer Physics Communications*, 2006, **174**, 704–727.

43 J. Wedekind, R. Strey and D. Reguera, *The Journal of Chemical Physics*, 2007, **126**, 134103.

44 G. Strobl, *Rev. Mod. Phys.*, 2009, **81**, 1287–1300.

45 Z. Wang, Z. Ma and L. Li, *Macromolecules*, 2016, **49**, 1505–1517.

46 W. Zhang and R. G. Larson, *The Journal of Chemical Physics*, 2019, **150**, 244903.

47 D. Parisi, J. Seo, B. Nazari, R. P. Schaake, A. M. Rhoades and R. H. Colby, *ACS Macro Letters*, 2020, **9**, 950–956.

48 D. A. Nicholson and G. C. Rutledge, *Polymer*, 2020, **200**, 122605.

49 W. Zhang and R. G. Larson, *Macromolecules*, 2020, **53**, 7650–7657.

50 D. Parisi, J. Seo, R. P. Schaake, A. M. Rhoades and R. H. Colby, *Progress in Polymer Science*, 2021, **112**, 101323.

51 S. Acierno and N. Grizzuti, *International Journal of Material Forming*, 2008, **1**, 583–586.

52 P. van Puyvelde, F. Langouche and J. Baert, *Int J Mater Form*, 2008, **1**, 667–670.

53 J. Seo, H. Takahashi, B. Nazari, A. M. Rhoades, R. P. Schaake and R. H. Colby, *Macromolecules*, 2018, **51**, 4269–4279.